Chinese Chemical Letters 35 (2024) 109131

Contents lists available at ScienceDirect

Chinese Chemical Letters

journal homepage: www.elsevier.com/locate/cclet

# Enhanced interfacial charge transfer on Bi metal@defective $Bi_2Sn_2O_7$ quantum dots towards improved full-spectrum photocatalysis: A combined experimental and theoretical investigation

Huizhong Wu[a,b], Ruiheng Liang[a,b], Ge Song[a,b], Zhongzheng Hu[a,b], Xuyang Zhang[a,b], Minghua Zhou[a,b,*]

[a] Tianjin Key Laboratory of Environmental Technology for Complex Trans-Media Pollution, College of Environmental Science and Engineering, Nankai University, Tianjin 300350, China
[b] Key Laboratory of Pollution Process and Environmental Criteria, Ministry of Education, College of Environmental Science and Engineering, Nankai University, Tianjin 300350, China

ARTICLE INFO

*Article history:*
Received 14 July 2023
Revised 14 August 2023
Accepted 18 September 2023
Available online 22 September 2023

*Keywords:*
Bi metal
$Bi_2Sn_2O_7$ quantum dots
Surface plasmon resonance
Oxygen vacancies

ABSTRACT

To mitigate the water pollution problem by photocatalytic degradation of typical antibiotics of tetracycline (TC), we prepared defective $Bi_2Sn_2O_7$ (BSO) quantum dots (QDs) with a full spectral response due to Bi metal deposition, using a one-pot hydrothermal method, labeled as Bi@BSO-OV. The optimized Bi@BSO-OV showed 73.4% removal of TC in 1 h under irradiation with a 50 W LED lamp in the wavelength band in the visible-near-infrared (vis-NIR) light, a rate that is substantially greater than that of pure BSO (14.7%). The synergistic interaction of Bi metal and oxygen vacancies (OVs) is crucial to boosting photocatalytic performance. The near-infrared region of the photo-response is extended by the surface plasmon resonance (SPR) effect of Bi metal, enhancing the photocatalytic performance and dramatically raising the efficiency of solar energy utilization. In addition to inducing defect levels in BSO, the OVs also activate the surface adsorbed $O_2$ to promote the production of $^{\bullet}O_2^-$ and $^1O_2$. DFT calculations reveal that Bi metal and OVs can mutually tune the charge transfer pathways. On the one hand, Bi metal can act as both a charge transfer bridge and an electron donor to assist charge separation. On the other hand, OVs-induced defect levels allow electrons that leap to the conduction band (CB) to first leap from the valence band (VB) to the defect levels, notably improving interfacial charge separation and transfer. The concept of design executed in this study for altering the catalyst by introducing both OVs and Bi metal can provide a rational design idea and potential insight for improving the photocatalytic activity for environmental applications.



Aside from its environmental friendliness and low cost, photocatalysis based on semiconductor materials is one of the most likely remedies to the environmental and energy crisis [1–3]. A variety of reactive oxygen species (ROS) are formed when the photogenerated electrons ($e^-$) and photogenerated holes ($h^+$) created by photocatalysts under the proper optical illumination interact with the $H_2O$ and $O_2$ adsorbed on the surface. Redox interactions between these ROS and water contaminants can result in the creation of products such as $CO_2$ and $H_2O$ [4–6]. However, an essential obstacle to practical applications is the discovery of efficient photocatalytic materials [7–10].

Due to their high stability, non-toxicity, controllable morphology, and economic benefits, $TiO_2$-based photocatalysts have been among the most researched photocatalysts in recent years [11,12]. In most cases, because of the wide band gap of $TiO_2$ (~3.2 eV), the utilization of solar radiation in photocatalysis is typically restricted, which mainly concentrates its light absorption range in the ultraviolet (UV) region. As a result, visible and near-infrared light, which account for about 43% and 50% of the total solar energy, respectively, cannot be exploited efficiently [13,14]. Light capturing, charge migration, and utilization. are the three dominant steps in the photocatalytic process [15,16]. Therefore, extending the photo-response region and suppressing the recombination of photogenerated $e^-$-$h^+$ pairs are two key issues in photocatalytic conversion.

* Corresponding author.
*E-mail address:* zhoumh@nankai.edu.cn (M. Zhou).

https://doi.org/10.1016/j.cclet.2023.109131
1001-8417/

Widely investigated in recent years is the degradation of organic contaminants employing bismuth-based photocatalytic materials [17], such as $H_2O$ photolysis [18], and $CO_2$ reduction [19], because of their optoelectronic properties and unique electronic structure [20]. In addition, the valence band (VB) of Bi-based semiconductor photocatalysts consists of Bi 6s and O 2p orbitals, which is more negative than that of other photocatalysts consisting of only O 2p orbitals, leading to a reduced band gap [21]. So far, many Bi-based photocatalysts such as $Bi_2O_3$ [22], BiOX (Cl, Br, and I) [23], bismuthates (*e.g.*, $BiVO_4$ [17], $Bi_2WO_6$ [24], and $Bi_2MoO_6$ [25]), and some other composite Bi-containing catalysts have been reported [25,26]. To further optimize the quantum efficiency of photocatalysts, surface defect construction, noble metal deposition, and heterostructure construction are well-established methods.

Noble metals deposited semiconductor structures are considered an attractive approach to enrich photocatalytic activity [27,28], because the surface plasmon resonance (SPR) effect of noble metals can broaden the light absorption range and improve photogenerated carrier separation efficiency [29,30]. Due to the intense absorption of light and collective electron oscillation of specific metals, SPR-generated hot carriers have the potential to be introduced into the adjacent semiconductor substrate for diverse reactions. So far, the augmentation of the photocatalytic efficiency in Bi-based semiconductors has involved the deposition of noble metals like Au, Ag, or Pt onto their surfaces. Significantly enhanced was the photocatalytic performance of $Pd/Bi_4O_5Br_2$ for bisphenol A removal when Zhu *et al.* constructed Pd nanoparticles deposited $Bi_4O_5Br_2$ nanosheets [31]. Shi *et al.* demonstrated that Ag quantum dots/$Bi_4O_5Br_2$ had excellent disinfection properties under UV irradiation, which was mainly due to the Schottky barriers generated by Ag formation and the synergistic effect of SPR improved the photo availability and separation efficiency of carriers [32].

Noble metals, however, are unsuitable for commercial applications as photocatalysts due to their scarce sources and high costs. In addition to noble metals, SPR of non-precious metal Bi may activate hot electrons, which can enhance the separation of $e^-$ from $h^+$ and thus have superior photocatalytic performance. In recent years, researchers have utilized self-deposited metal Bi on the surface of Bi-based photocatalysts such as $Bi_4O_5I_2$ [33], BiOCl [34], $Bi_2MoO_6$ [35], and $Bi_2SiO_5$ [36] to enhance their light absorption capability and improve the efficiency of photogenerated carrier separation. By using an *in-situ* thermal treatment approach, Huang *et al.* created $Bi^0$/OVs-$(BiO)_2CO_3$ with outstanding selectivity for photocatalytic NO elimination [37]. The earlier research showed that, in comparison to a single Bi-based semiconductor, the deposition of metals produced by the SPR effect and OVs exhibited noticeably increased photocatalytic activity. The photocatalytic degradation of aqueous pollutants under near-infrared (NIR) light irradiation benefited from the synergistic effect of the SPR effect and the generation of oxygen vacancies (OVs). The detailed revelation of the interfacial electronic structure and the microscopic mechanism of charge transfer remain to be explored. Featuring the interaction between Bi 6s and O 2p orbitals, pyrochlore $Bi_2Sn_2O_7$ (BSO) exhibits a dispersed VB and a smaller band gap, consisting of $BiO_4$ tetrahedra and $SnO_6$ octahedra. This interaction facilitates the migration of photogenerated carriers [38,39]. The preparation of $Bi_2Sn_2O_7$ with quantum size, adjustable band gap, and large intrinsic dipole moments for improved visible-near-infrared (vis-NIR) light responsiveness and quick charge separation is another accomplishment of this work [40].

Herein, we introduce a hydrothermal chemical reduction method that enables the one-step preparation of Bi-deposited BSO quantum dots (QDs), labeled as Bi@BSO-OV, featuring abundant OVs. It is expected that the combination of Bi metal and BSO will develop a catalyst structure suitable for broadband photo-response, and promote the separation and migration ability of $e^-$ and $h^+$ to enhance photocatalytic activity. On the one hand, the formation of a significant amount of ROS is facilitated by the presence of OVs, enabling molecules' adsorption and electron transfer. On the other hand, the improved carrier separation and full spectral absorption because of the interfacial architecture and SPR effect of Bi make the Bi@BSO-OV catalyst structure excellent for photocatalytic degradation of tetracycline (TC). A description of TC is available in Supporting information. This study investigated the enhanced performance of Bi@BSO-OV by conducting comprehensive characterization, degradation tests, active substance capture studies, band structure analysis, and theoretical calculations based on first principles theory. In addition to offering prospective and useful insights for upcoming applications of photocatalytic degradation of pollutants, this study offers a straightforward and affordable way the creation of effective photocatalysts with full-spectrum reactions.

One-pot hydrothermal preparation was used to create the defective BSO QDs nanoparticles that were decorated by the Bi metal. First, 15 mL of 2 mol/L diluted $HNO_3$ was added 0.49 g of $Bi(NO_3)_3{\cdot}5H_2O$ to produce A. Solution B was formed by dispersing 0.21 g of $Na_2SnO_3$ and 0.36 g of polyvinylpyrrolidone (PVP) in 15 mL of deionized water. Then, add B solution dropwise to A solution, add an appropriate amount of glucose, stir magnetically for 30 min, and adjust the pH value to 12 with NaOH solution (1 mol/L). The final product was obtained by transferring it to a 100 mL Teflon-lined autoclave and heating it at 180 °C for 24 h. Subsequently, it was allowed to cool naturally to room temperature, washed three times with deionized water and ethanol, and dried for 12 h at 80 °C. Based on the mass ratio of glucose to $Bi(NO_3)_3{\cdot}5H_2O$, the samples were identified as Bi@BSO-X, where X is one of 20, 30, 50, or 70. The samples without glucose were labeled as BSO. In the subsequent degradation experiments, we found that Bi@BSO-50 showed higher performance in degrading TC compared to Bi@BSO-X (X = 20, 30, 70), therefore, we chose Bi@BSO-50 as the representative for the following characterization measurements.

Fig. 1a illustrates the results of the XRD analysis conducted on the prepared samples, BSO and Bi@BSO-X, to examine their crystal structures and phases. It can be observed that the peaks of pure BSO are well-matched with cubic phase BSO (JCPDS No. 88-0496). For the Bi@BSO-X samples, diffraction peaks of Bi metal (JCPDS No. 85-1331) were observed at 27.2°, 38.1°, and 39.7°, in addition, it is gradually intensified with the increase of glucose amount. This demonstrated that during the hydrothermal process, glucose reduced a portion of $Bi^{3+}$ to Bi metal. Notably, the presence of diffraction peaks broadening can be indirectly attributed to the formation of defects when using glucose as a reductant [41].

XPS was employed to further characterize the elemental composition and chemical state of the samples. Both the BSO and Bi@BSO-50 samples exhibit a coexistence of Bi, Sn, and O elements, as shown in the XPS survey spectra (Fig. S1 in Supporting information), which provide a comprehensive scanning of the full spectrum. The high-resolution XPS scan spectra of the Bi 4f area are shown in Fig. 1b. It has two notable distinctive peaks at 158.8 eV and 164.1 eV that are ascribed to the Bi $4f_{7/2}$ and Bi $4f_{5/2}$ orbitals of $Bi^{3+}$, respectively [42]. The reduced binding energy at the peak of $Bi^{3+}$ in Bi@BSO-50 compared to pure BSO can be attributed to the structural changes on the Bi@BSO-50 surface due to the presence of OVs or Bi metal [43]. More crucially, the rising electron cloud density that results from the falling binding energy might enhance electronic activity. Additionally, two peaks were seen at 156.1 and 161.9 eV which is caused by the zero-valent metal $Bi^0$ [44,45], which is in line with the XRD findings and infers indirectly that the generation of Bi metal on the surface of BSO. XPS peaks of Sn 3d (Fig. 1c) are attributed to Sn $3d_{3/2}$ and Sn $3d_{5/2}$, respectively, and are positioned at 494.5 and 486.2 eV, respectively [46]. From Fig. 1d, it can be seen that there is a Bi-O bond peak at ~529.6 eV,

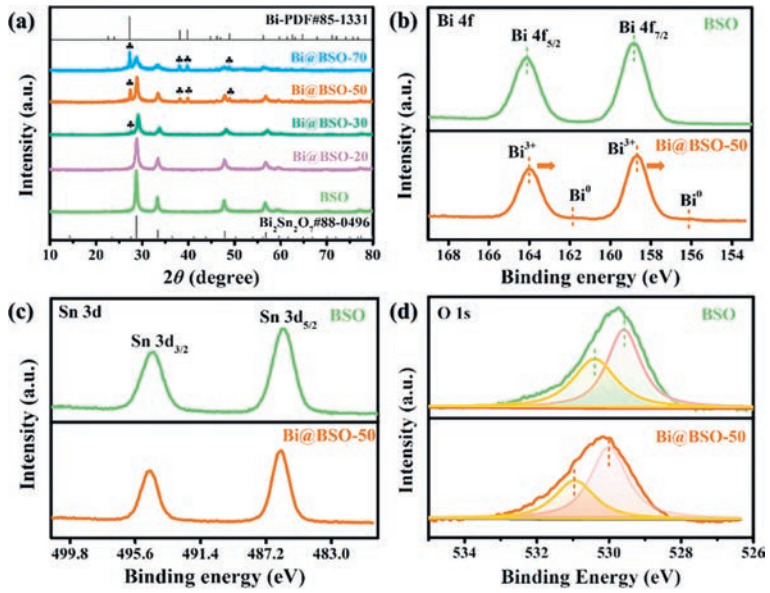


**Fig. 1.** (a) XRD patterns of BSO and Bi@BSO-X. XPS spectra of BSO and Bi@BSO-X: Bi 4f (b), Sn 3d (c), and O 1s (d).

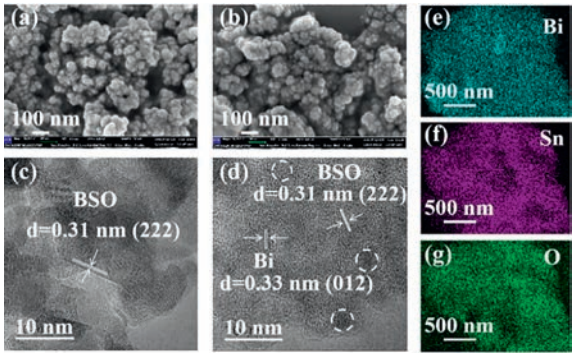


**Fig. 2.** SEM images of BSO (a) and Bi@BSO-50 (b). HRTEM images of BSO (c) and Bi@BSO-50 (d). The corresponding Bi (e), Sn (f), and O (g) EDS elemental mapping images of Bi@BSO-50.

and the binding energy of the Bi-O bond is enhanced in Bi@BSO-50, which further proves that Bi had a strong interaction with O. The other shoulder peak in the O 1s spectrum at 530.4 eV corresponds to the adsorbed $H_2O$ [47].

The synthesized powders were characterized morphologically and microstructurally using SEM. According to Fig. 2a, the natural BSO presented a morphology of irregular spherical cluster structure formed by the agglomeration of small particles. The average size of $Bi_2Sn_2O_7$, observed in Fig. S2 (Supporting information), falls within the range of QDs sizes, approximately measuring 6.23 nm. The morphology of the Bi@BSO-50 sample shown in Fig. 2b did not change significantly after the reduction of the Bi metal. Fig. 2c shows the clear lattice stripes of the pure BSO sample with a distance of 0.31 nm between the lattice stripes, which is in good agreement with the BSO (222) crystal plane on the standard PDF card. Fig. 2d shows the BSO sample with Bi metal decoration, and the distinct lattice stripes of BSO and Bi can be observed simultaneously. The stripes observed, with a lattice distance of 0.33 nm, are ascribed to the (012) crystalline plane of Bi metal. The energy dispersive spectroscopy (EDS) analysis showed that the elements Bi, Sn and O were homogeneously distributed on the Bi@BSO-50 surface (Figs. 2e-g).

Broad-spectrum light absorption properties are a prerequisite for the efficient use of light, which necessitates the use of UV-vis diffuse reflectance spectrophotometer (DRS) to research photon absorption characteristics. The optical absorption analysis of the BSO and Bi@BSO-X samples was carried out using UV-vis DRS as depicted in Fig. 3a. As the Bi content increases, the vis-NIR absorption of Bi@BSO-X samples significantly enhanced, while the absorption edge of pure BSO remains at 420 nm. A near-infrared absorption band near 800 nm was present in all of the Bi@BSO-X samples, which can be attributed to the SPR and light scattering of Bi metal [48]. In these samples of Bi@BSO-X, the metal Bi can concentrate the incident photon energy into the plasmonic excitonic oscillations, thus significantly enhancing the electromagnetic field and thus promoting the separation of $e^-$ and $h^+$ [49–51]. Moreover, the existence of OVs can also broaden the range of optical absorption for the photocatalysts. The decoration of $Bi^0$ and OVs effectively improves the light absorption capacity, consequently, enhances the photocatalytic performance for TC removal, thus highlighting the synergistic interaction. The band gaps of BSO and Bi@BSO-50 were determined to be 2.42 eV and 2.09 eV, respectively, based on the intercepts of the tangents to the plots of $(\alpha hv)^{1/2}$ *vs.* photoenergy in Fig. 3b, and the band gaps of Bi@BSO-20 and Bi@BSO-70 are shown in Fig. S3 (Supporting information). Combining the XPS valence spectra (Fig. S4 in Supporting information) of BSO and Bi@BSO-50, the addition of Bi metal has no discernible impact on the VB, both at 1.72 eV. According to the equation, $E_{CB} = E_{VB} - E_g$, −0.7 and −0.37 eV are the CB positions of BSO and Bi@BSO-50, respectively, where $E_{VB}$ is VB edge potential, $E_{CB}$ is CB edge potential, $E_g$ is the band gap. The CB of Bi@BSO-50 exhibits a more negative potential than the potential for generating superoxide radicals ($E^0(O_2/{}^{\bullet}O_2^-$, −0.33 eV *vs.* NHE), while its VB displays a positive potential compared to the potential for generating hydroxyl radicals $E^0(OH^-/{}^{\bullet}OH$, 1.99 eV *vs.* NHE) [52].

The efficiency of $e^-$-$h^+$ separation can be assessed through PL spectra. Fig. 3c shows the PL spectra of the prepared sample. The presence of Bi metal induces an electromagnetic field through the SPR effect, resulting in a significantly lower photoluminescence (PL) intensity for Bi@BSO-X compared to pure BSO. This effect is more effective in accelerating the interfacial charge transfer efficiency, further reflecting the phenomenon of reduced photogenerated $e^-$-$h^+$ recombination and promoted charge transfer [53]. The electron paramagnetic resonance (EPR) signal at $g = 2.003$ observed in Fig. 3d, particularly for the Bi@BSO-50 sample, indicates the presence of electrons trapped on OVs.

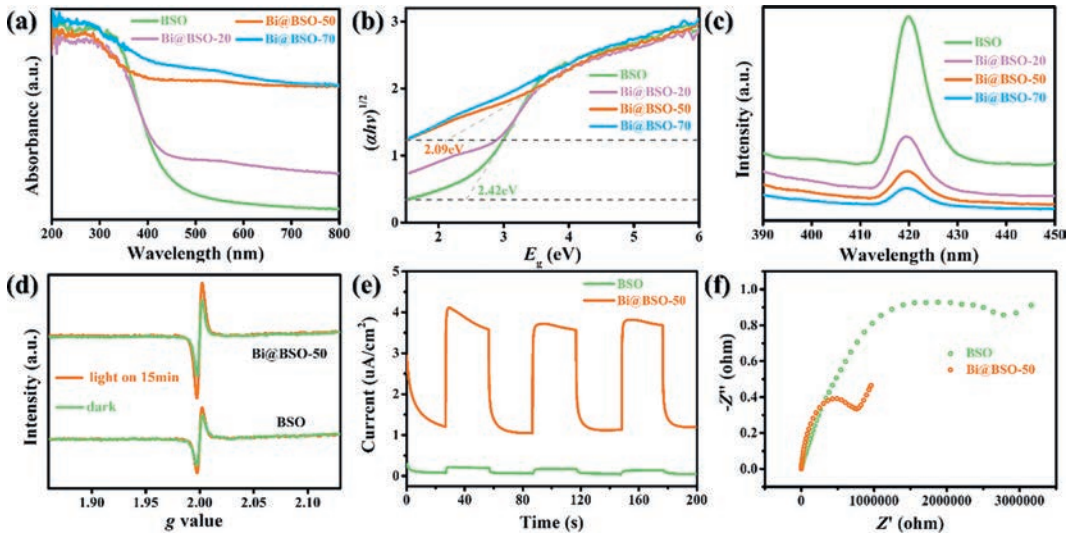


**Fig. 3.** (a) UV-vis DRS of BSO and Bi@BSO-X. (b) the bang gap of BSO and Bi@BSO-X. (c) Room-temperature PL spectra of BSO and Bi@BSO-X. (d) EPR spectra of BSO and Bi@BSO-50. (e) Photocurrent transient response curves of BSO and Bi@BSO-50. (f) EIS Nyquist plots of BSO and Bi@BSO-50.

To examine the separation effectiveness of photogenerated carriers in Bi@BSO-X, transient photocurrent response and electrochemical impedance spectroscopy (EIS) were studied. These analyses provide insights into the primary influence of the rapid separation and transfer of carriers on photocatalytic performance. Fig. 3e displays the transient photocurrent intensity of BSO and Bi@BSO-50 when subjected to vis-NIR light irradiation. Compared with pure BSO, the photocurrent intensity of Bi@BSO-50 is significantly enhanced, nearly 20 times that of natural BSO. Since the presence of Bi metal does improve the utilization of vis-NIR light, the issue of low electron utilization and high charge recombination rate of BSO is solved. In the Nyquist plot, the resistance of the Bi@BSO-50 (28.6 Ω) was much reduced compared to BSO (325.7 Ω) (Fig. 3f), suggesting that the introduction of Bi metal results in higher interfacial charge transfer efficiency and lower carrier migration resistance of the prepared photocatalysts. The synergistic interaction between plasma Bi and OVs is responsible for the increased photocurrent and decreased resistance, which suggests efficient transport of photogenerated carriers on Bi@BSO-OV.

In an attempt to fully understand the effect of the structural features of Bi@BSO-OV on the photocatalytic ability, the interfacial charge transfer was analyzed using DFT. The charge difference distribution of the BSO and Bi metal layers is shown in Fig. 4a. Apparently, the charge density difference occurs mainly at the interface between BSO and Bi metal, and the Bi-O layer of BSO acquires an abundance of electrons from Bi element and serves as a photoactive site. The electronic location function (ELF) depicted in Fig. 4b demonstrates a strong covalent connection between the metal Bi and Bi-O layers on the BSO surface, which facilitates a charge transfer channel from Bi metal to BSO. Calculations were performed to determine the potentials of Bi@BSO-OV and BSO, aiming to examine the ease with which the excited electrons of Bi can be transported to the Bi-O layer. Fig. 4c represents the Bi metal layer potential (-14.70 eV) is 12.54 eV higher than the O element layer (-27.24 eV) of BSO. The hot electrons produced by the Bi metal can easily transcend the potential barrier to the neighboring Bi-O layer when exposed to vis-NIR light. The density of states (DOS) of pure BSO and Bi@BSO-OV were calculated as shown in Fig. 4d. The EPR results are compatible with the generation of defect levels between the band gap of Bi@BSO-OV. Moreover, the work functions of Bi metal and BSO were calculated and estimated to be 4.38 eV and 4.89 eV, respectively, as illustrated in Figs. 4e and f. The observation suggests that the Fermi level of Bi metal is positioned higher than that of BSO. In this case, when Bi metal contacts BSO, the electrons in Bi metal can flow to BSO until the Fermi levels are in equilibrium. Subsequently, hot electrons on the Bi metal spontaneously migrate to the CB of BSO under vis-NIR light irradiation driven by the excitation electric field, achieving effective separation of $e^-$-$h^+$ pairs. Within this system, the introduction of Bi metal has a great impact on enhancing vis-NIR light absorption in addition to acting as an acceptor and donor of photogenerated electrons to promote charge transfer. The OVs of BSO can also enhance the electron-giving ability of Bi@BSO-OV by separating the photogenerated $e^-$-$h^+$ pairs. Hence, the combined effect of the Bi metal's SPR and the presence of oxygen vacancies can account for the elevated photocatalytic activity exhibited by Bi@BSO-OV photocatalysts.

Under vis-NIR light irradiation, the fabricated samples were examined for the photocatalytic removal performance for TC, as displayed in Fig. 5a. As the amount of Bi deposited on the surface increased, the degradation efficiency of TC exhibited a pattern of initial increase followed by a subsequent decrease, in which Bi@BSO-50 showed the highest TC removal rate of 73.4% within 1 h, followed by Bi@BSO-30 (56.8%), Bi@BSO-70 (45.7%), Bi@BSO-20 (32.9%) and BSO (14.7%), the corresponding kinetic data were 0.0236, 0.0156, 0.0101, 0.0076 and 0.0028 $min^{-1}$, respectively. In addition, the adsorption performance of the Bi@BSO-50 catalyst is shown in Fig. S5 (Supporting information), which can adsorb 14.8% of TC under dark conditions for 1 h. The synergistic interaction between Bi metal and OVs considerably improved the vis-NIR photocatalytic performance of Bi@BSO-50. On the one hand, the SPR effect of Bi metal can boost the separation of photogenerated $e^-$-$h^+$ pairs and increase the efficiency of vis-NIR light absorption. On the other hand, under vis-NIR light irradiation, the OVs facilitate the electron leap from the VB to the defect levels and then to the CB [54,55]. Despite Bi@BSO-70 displaying the highest light absorption and efficient separation of photogenerated charges, the structural integrity of its substrate collapses when subjected to excessive reductant treatment, resulting in fewer reactive sites for BSO exposure to TC and hindering the photocatalytic effect.

The removal effect of Bi@BSO-50 dosage was evaluated in the range of 100-400 mg/L, as shown in Fig. 5b. When the amount of Bi@BSO-50 was increased from 100 mg/L to 300 mg/L, the removal rate of TC was significantly increased after 60 min, and the *pseudo-*

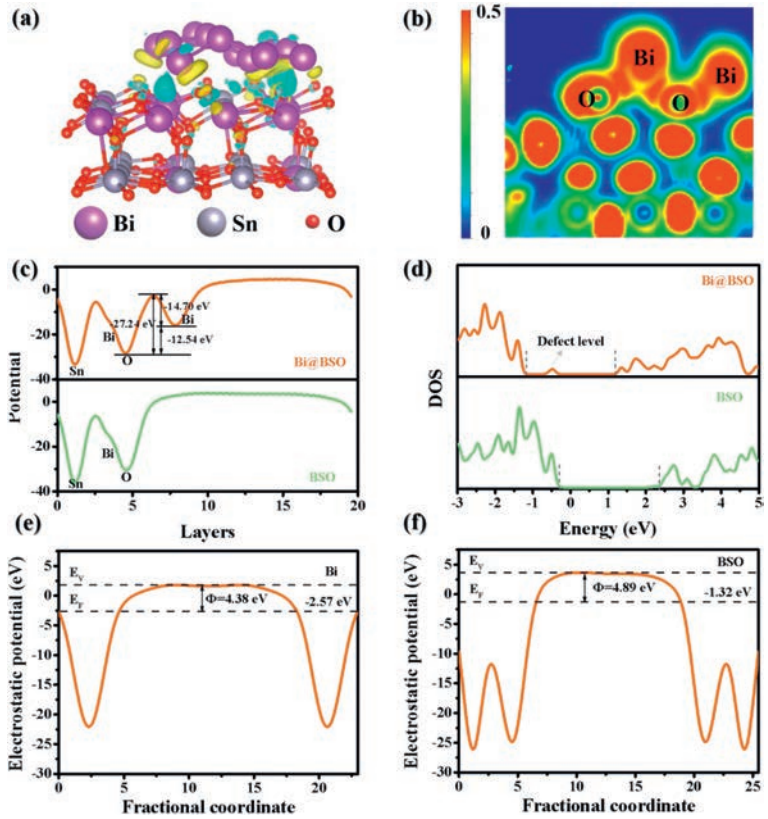


**Fig. 4.** (a) Charge difference distribution of Bi@BSO-OV: Charge depletion is in yellow and charge accumulation is in blue. (b) Electronic location function (ELF) of Bi@BSO-OV. (c) Electrostatic potential. (d) Calculated DOS of BSO and Bi@BSO-OV. The electrostatic potentials of Bi metal (e) and BSO (f).

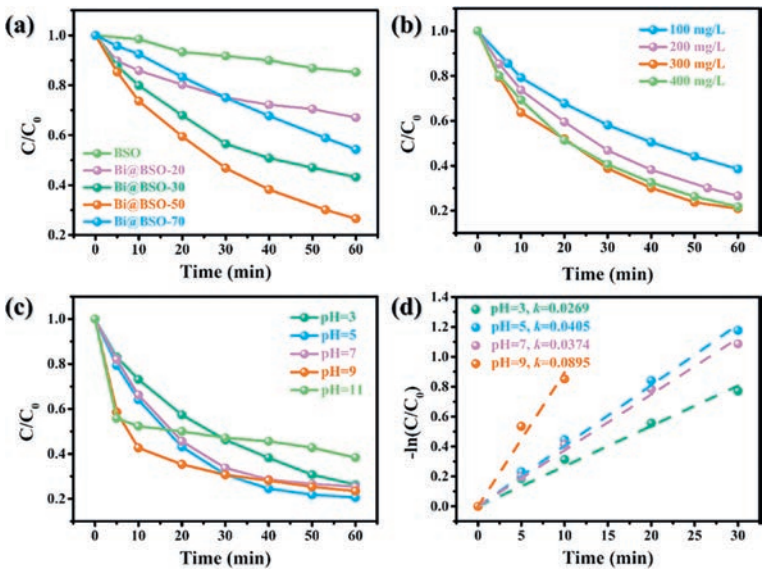


**Fig. 5.** (a) TC photocatalytic degradation efficiency of BSO and Bi@BSO-X. Effects of Bi@BSO-50 amount (b), and initial pH (c) on the degradation performance of TC under vis-NIR light illumination. (d) Apparent rate constants of Bi@BSO-50 at different initial pH.

first-order rate constant increased from 0.0167min$^{-1}$ to 0.0285 min$^{-1}$ (Fig. S6 in Supporting information). While the degradation efficiency did not change even when the catalyst amount was further raised from 300 mg/L to 400 mg/L ($k = 0.0272$ min$^{-1}$). This is a consequence of the fact that the more catalysts there are, the higher the turbidity of the solution, which may disperse the light and reduce the effect of light passing through the solution [56]. Considering the removal effect and economy, the optimal dosage of BSO was selected as 300 mg/L in the continuous experiment.

The initial pH of the solution is a critical factor in the photocatalytic process as it impacts the surface charge properties of the photocatalyst and regulates the ionization state of the catalyst surface, thereby influencing the degradation and adsorption capacity

of targeted organic compounds. The capacity of the compound for adsorption and dissociation, the oxidation potential of the VB, and the distribution of charges on the catalyst surface are all impacted by the pH level. As shown in Fig. 5c, at pH 11, Bi@BSO-50 showed poor photocatalytic degradation of TC, with only 61.6% degradation for 1 h. Fig. 5d shows the degradation efficiency for TC at pH 3, 5, 7, and 9 was $k_{pH9}$ (0.0895 $min^{-1}$) > $k_{pH5}$ (0.0405 $min^{-1}$) > $k_{pH7}$ (0.0374 $min^{-1}$) > $k_{pH3}$ (0.0269 $min^{-1}$). The p$K_a$ values of TC were 3.3, 7.7, 9.7, and 12 [57], mainly for $H_4TC^+$, $H_3TC$, and $H_2TC^-$ at pH 3, 7 and 9, respectively [58]. Particles in aqueous solutions that are solid have a property known as the pH of the point of zero charge ($pH_{PZC}$). The surface charge of solid particles is neutral at this pH. pH < $pH_{PZC}$ gives a positive surface charge and pH > $pH_{PZC}$ gives a negative surface charge. The $pH_{PZC}$ of Bi@BSO-50 is 7.6 (Fig. S7 in Supporting information). Therefore, Bi@BSO-50 is negatively charged at pH 9 and 11, while it is positively charged at pH 3, 5, and 7. The electrostatic repulsion between positively charged Bi@BSO-50 and $H_4TC^+$ is enhanced at pH 3 and 5, inhibiting TC adsorption on it. Neutral TC molecules seemed to be attracted to the positively charged Bi@BSO-50 surface at pH 7, but the solution pH was close to the $pH_{PZC}$ of Bi@BSO-50, leading to their aggregation and slightly reducing the catalytic activity [59]. At pH 11, the electrostatic repulsion between the dominant $H_2TC^-$ and $HTC^{2-}$ and the negatively charged catalyst is enhanced, inhibiting the TC adsorption on the catalyst surface and leading to poorer performance at the initial solution pH 11. Furthermore, because of the high electrical density of their ring system, negatively charged TC molecules have the propensity to attract electrophilically -OH [57], thus enhancing the photocatalytic activity under alkaline conditions. Apparently, the adsorption mechanism and -OH content may affect the ideal circumstances for TC photocatalytic degradation. Slightly alkaline pH conditions promoted the photocatalytic degradation of TC in the current investigation. Furthermore, the comparison between Bi@BSO-50 and other photocatalysts in previous work for TC degradation is presented in Table S1 (Supporting information).

Furthermore, by using different scavengers, 10 mmol/L methanol (MeOH, $^{\bullet}OH$ scavenger), 10 mmol/L furfuryl alcohol (FFA, $^1O_2$ scavenger), 9000 U/L superoxide dismutase (SOD, $^{\bullet}O_2^-$ scavenger), and 10 mmol/L triethanolamine (TEOA, hole consuming agent), the primary reactive species involved in the photocatalytic process were investigated using reactive species trapping studies (Fig. 6a). The introduction of FFA significantly inhibited the photodegradation performance of TC, indicating that $^1O_2$ is the primary active substance engaged in photocatalysis. Moreover, the inclusion of TEOA led to a decrease in the photocatalytic degradation of TC, lowering it from 76.5% to 64.5%, demonstrating that $h^+$ is also involved in the degradation of TC. The photocatalytic activity of Bi@BSO-50 was not substantially impacted by the addition of MeOH or SOD, proving that $^{\bullet}OH$ and $^{\bullet}O_2^-$ radicals do not contribute to the degradation process. However, we detected the presence of $^{\bullet}O_2^-$ in EPR experiments (Fig. S8 in Supporting information), and due to the extremely low redox potential of $^{\bullet}O_2^-$ ($E^0 = -0.33$ V (*vs.* NHE)) and the exceedingly rare possibility of direct TC degradation with $^{\bullet}O_2^-$, the addition of SOD did not prevent the degradation of TC. However, $^{\bullet}O_2^-$ is a vital precursor for the formation of $^1O_2$ [60,61]. The EPR spin-trapping technique was used to further confirm the reactive species that participated in photocatalytic degradation under dark and visible light. As shown in Fig. 6b, the electron sacrificial agent of Bi@BSO-50 is rapidly depleted under light irradiation, but it is still residual for BSO. It indicates that the Bi@BSO-50 catalyst has more free electrons because $e^-$ can migrate from the Bi metal to the CB of BSO under vis-NIR light irradiation, thereby preventing the recombination of $e^-$-$h^+$ pairs. In Fig. 6c, the Bi@BSO-50 sample shows a strong $^1O_2$ signal, which is generated by the reduction of oxygen. Furthermore, DFT calculations were used to examine the adsorption energy of $O_2$ molecules on the surface BSO with or without OVs. The surface adsorption energy of perfect BSO is −0.35 eV, which is lower than that in the presence of OVs (−0.46 eV). The larger adsorption energy indicates that the OVs promote the adsorption and activation of $O_2$ molecules on the catalyst surface.

For the catalysts to be used effectively in the treatment of organic contaminants for their practical application, stability and, reusability are crucial. Five rounds of Bi@BSO-50 degradation of TC were conducted under the same experimental circumstances. The photocatalytic activity of the material was well maintained, but after five rounds of experiments, the catalyst exhibited a slight deactivation and the degradation efficiency of TC declined from 76.5% to 65.7% within 1 h, as shown in Fig. 6d, which may be the result of the accumulation of intermediates on the surface of the catalyst. It demonstrated the excellent stability and reuse potential of Bi@BSO-50 in degrading TC in wastewater.

The photocatalytic mechanism corresponding to Bi@BSO-OV, which was created by combining various experimental and theoretical findings, consists of five primary steps, as illustrated in Fig. 7. As seen in process I, the OVs in BSO cause the formation of defect levels, enabling a direct transition of photogenerated $e^-$ from VB to defect levels when exposed to vis-NIR light. This also allows the defective BSO to have enhanced vis-NIR photocatalytic activity, as electrons from the defect levels can be further hopped to the CB of the BSO (process II). In addition, the incorporation of Bi metal on BSO has an appreciable contribution to its vis-NIR light photocatalytic performance. Firstly, an electromagnetic field can be generated by the SPR effect of Bi element, which drives the defective BSO with higher excited state electrons to gather in valence band maximum (VBM), which facilitates the separation of photogenerated $e^-$-$h^+$ pairs (process III). Secondly, hot electrons of Bi elements are transferred to the Bi-O layer (process IV), and electrons of defect levels are transferred to Bi elements while maintaining the neutrality of Bi elements (process V), which promotes the $e^-$-$h^+$ pairs separation of BSO and increases the generation of radicals. Consequently, the photocatalytic performance can be significantly improved by *in situ* reduction of $Bi^{3+}$ to $Bi^0$ and by creating defects in the QDs structure of BSO.

To conclude, a facile hydrothermal chemical reduction method was employed to fabricate the defective Bi@BSO photocatalyst. The photocatalytic degradation performance of TC exhibited a significant improvement under vis-NIR irradiation, because of the synergistic effect of OVs and the SPR of Bi, surpassing that of pure BSO. Bi metal not only broadens the photo-response range in the vis-NIR region, but it can promote carrier separation efficiency and provide more hot electrons. In the meantime, the created OVs can take advantage of the separation of photogenerated carriers and optimize the band gap, thus promoting the generation of ROS. Furthermore, electrochemical measurements confirmed the high interfacial charge transfer efficiency and low carrier migration resistance of BSO modified with $Bi^0$ and OVs. The correlated reaction mechanism of photocatalytic degradation of TC on Bi@BSO-OV was suggested by combining radical trapping and DFT calculations, and the important role of the synergistic interaction of OVs and Bi metal was elucidated. This work offers novel insights into the design of non-precious metal-based photocatalysts, which further provides potential and practical insights for future applications of photocatalytic degradation of pollutants.

## Declaration of competing interest

The authors declare that they have no known competing financial interests or personal relationships that could have appeared to influence the work reported in this paper.

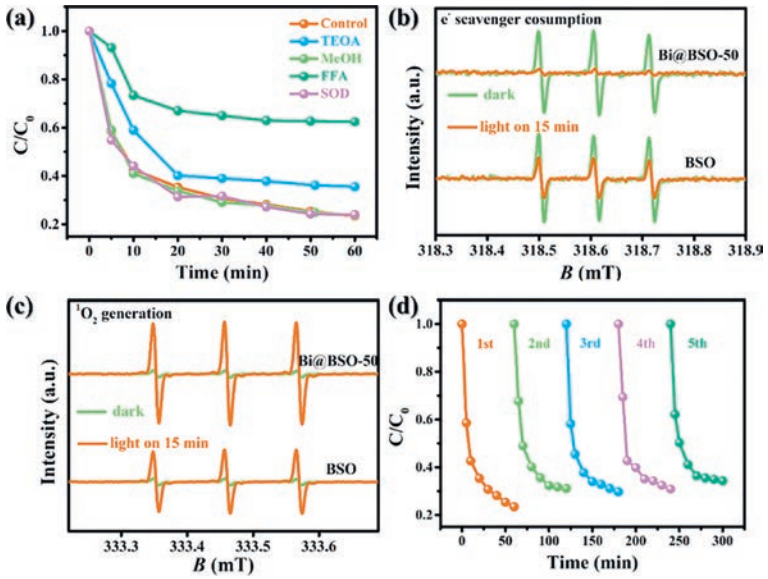


**Fig. 6.** (a) Reactive species trapping experiments: Experimental conditions: initial TC concentration = 20 mg/L, initial pH = 9. EPR spectra of TEMPO-$h^+$ adduct (b) and DMPO-$^1O_2$ adduct (c) for BSO and Bi@BSO-50. (d) Recycling tests of Bi@BSO-50.

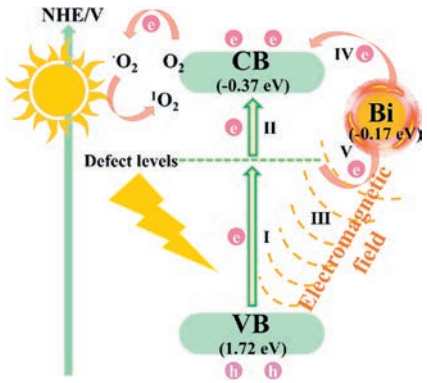


**Fig. 7.** Schematic diagram of the photocatalytic mechanism of Bi@BSO-OV under light irradiation.

## Acknowledgments

This work was financially supported by the Key Project of Natural Science Foundation of Tianjin (No. 21JCZDJC00320), National Key R&D Program International Cooperation Project (No. 2021YFE0106500), Tianjin Development Program for Innovation and Entrepreneurship, and Fundamental Research Funds for the Central Universities, Nankai University.

## Supplementary materials

Supplementary material associated with this article can be found, in the online version, at doi:10.1016/j.cclet.2023.109131.

## References

[1] S. Huang, F. Feng, R.T. Huang, et al., Adv. Mater. 34 (2022) 2208438.
[2] K.L. Zhang, M. Dan, J.F. Yang, et al., Adv. Funct. Mater. 33 (2023) 2302964.
[3] W. Cui, J.Y. Li, F. Dong, ACS EST Eng. 2 (2022) 1103–1115.
[4] R Hailili, Z.Q. Wang, H. Ji, et al., Environ. Sci. Nano 9 (2022) 1453–1465.
[5] P.F. Zhu, X.H. Yin, X.H. Gao, et al., Chin. J. Catal. 42 (2021) 175–183.
[6] M.L. Shi, B. Rhimi, K Zhang, et al., Chemosphere 275 (2021) 130083.
[7] P.K. Verma, Coordin. Chem. Rev. 472 (2022) 214805.
[8] Y.Q. He, Q. Lei, C.G. Li, et al., Mater. Today 50 (2021) 358–384.
[9] Q. Lei, S.J. Yang, D.H. Ding, et al., J. Mater. Chem. A 9 (2021) 2491–2525.
[10] B. Samanta, Á. Morales-García, F. Illas, et al., Chem. Soc. Rev. 51 (2022) 3794–3818.
[11] S. Chen, Y.X. Li, C.Y. Wang, RSC Adv. 5 (2015) 15880–15885.
[12] R.H. Liang, Z.Z. Hu, H.Z. Wu, et al., Sep. Purif. Technol. 314 (2023) 123591.
[13] T. Ohno, M. Akiyoshi, T. Umebayashi, et al., Appl. Catal. A: Gen. 265 (2004) 115–121.
[14] Z.Z. Hu, M.H. Zhou, H.A. Maitlo, et al., Appl. Catal. B: Environ. 331 (2023) 122676.
[15] L. Buzzetti, G.E.M. Crisenza, P. Melchiorre, Angew. Chem. Int. Ed. 58 (2019) 3730–3747.
[16] C.Y. Cheng, Q.H. Liang, M. Yan, et al., J. Hazard. Mater. 424 (2022) 127721.
[17] H. Du, W.H. Pu, Y.Y. Wang, et al., J. Alloy. Compd. 787 (2019) 284–294.
[18] S.L. Bai, J.Y. Han, K.W. Zhang, et al., Int. J. Hydrogen Energ. 47 (2022) 4375–4385.
[19] T. Ouyang, Y.T. Ye, C.H. Tan, et al., J. Phys. Chem. Lett. 13 (2022) 6867–6874.
[20] F. Hasanvandian, M. Moradi, S.A. Samani, et al., Chemosphere 287 (2022) 132273.
[21] B. Li, L.C. Nengzi, R.N. Guo, et al., Chin. Chem. Lett. 31 (2020) 2705–2711.
[22] J.S. Gao, S.S. Rao, X.H. Yu, et al., J. Colloid Interf. Sci. 628 (2022) 166–178.
[23] M. Yadav, S. Garg, A. Chandra, et al., Ceram. Int. 45 (2019) 17715–17722.
[24] Y.R. Lv, Z.L. Wang, Y.X. Yang, et al., J. Hazard. Mater. 432 (2022) 128665.
[25] Y.Q. Lu, C.S. Ding, J. Guo, et al., J. Alloy. Compd. 924 (2022) 166533.
[26] Z.P. Ma, L. Zhang, X. Ma, et al., Sep. Purif. Technol. 297 (2022) 121435.
[27] A. Zada, P. Muhammad, W. Ahmad, et al., Adv. Funct. Mater. 30 (2020) 1906744.
[28] E.E. Elemike, D.C. Onwudiwe, L. Wei, et al., Sol. Energ. Mat. Sol. C 201 (2019) 110106.
[29] R.S. Haider, S. Wang, Y. Gao, et al., Nano Energy 87 (2021) 106189.
[30] S. Li, Z.C. Zhao, M.S. Liu, et al., Nano Energy 95 (2022) 107031.
[31] N. Li, G.Q. Zhu, M. Hojamberdiev, et al., J. Photoch. Photobio. A 356 (2018) 440–450.
[32] H.X. Shi, W. Wang, L.H. Zhang, et al., J. Environ. Chem. Eng. 9 (2021) 105867.
[33] L.P. Chen, C.E. Li, Y.F. Zhao, et al., Chem. Eng. J. 425 (2021) 131599.
[34] L.S. Wang, H.S. Yin, S. Wang, et al., Appl. Catal. B: Environ. 305 (2022) 121039.
[35] L. Geng, W.J. Li, X.T. Liu, et al., J. Colloid Interf. Sci. 629 (2023) 723–732.
[36] X.S. Guan, X.C. Zhang, C.M. Zhang, et al., Compos. Commun. 20 (2020) 100366.
[37] F Rao, G.Q. Zhu, W.B. Zhang, et al., Appl. Catal. B: Environ. 281 (2021) 119481.
[38] M. Benčina, M. Valant, J. Am. Ceram. Soc. 101 (2018) 82–90.
[39] B. Allured, S. DelaCruz, T. Darling, et al., Appl. Catal. B: Environ. 144 (2014) 261–268.
[40] Z.P. Yan, W.C. Wang, L.L. Du, et al., Appl. Catal. B: Environ. 275 (2020) 119151.
[41] R. Xu, Z.W. Xu, Y.C. Si, et al., ACS Appl. Mater. Inter. 12 (2020) 36917–36927.
[42] W.M. Huang, X. Hua, Y.P. Zhao, et al., J. Mater. Sci. Mater. El. 30 (2019) 14967–14976.
[43] X.W. Li, W.D. Zhang, J.Y. Li, et al., Appl. Catal. B: Environ. 241 (2019) 187–195.
[44] Y. He, J.Y. Li, K.L. Li, et al., Chin. J. Catal. 41 (2020) 1430–1438.
[45] J.L. Lv, J.F. Zhang, J. Liu, et al., ACS Sustain. Chem. Eng. 6 (2018) 696–706.
[46] X. Chen, B.H. Zhou, S.L. Yang, et al., RSC Adv. 5 (2015) 68953–68963.
[47] S.H. Ma, X. Luo, G. Ran, et al., Chem. Eng. J. 435 (2022) 134810.
[48] Y.X. Gao, Y. Huang, Y. Li, et al., ACS Sustain. Chem. Eng. 4 (2016) 6912–6920.
[49] M.L. Brongersma, N.J. Halas, P. Nordlander, Nat. Nanotechnol. 10 (2015) 25–34.

[50] G.M. Jiang, X.W. Li, M.N. Lan, et al., Appl. Catal. B: Environ. 205 (2017) 532–540.
[51] S.K. Cushing, J.T. Li, F.K. Meng, et al., J. Am. Chem. Soc. 134 (2012) 15033–15041.
[52] W.K. Jo, T.S. Natarajan, ACS Appl. Mater. Interfaces 7 (2015) 17138–17154.
[53] Y.J. Sun, Z.W. Zhao, F. Dong, et al., Phys. Chem. Chem. Phys. 17 (2015) 10383–10390.
[54] F. Dong, T. Xiong, S.J. Yan, et al., J. Catal. 344 (2016) 401–410.
[55] T. Stauber, N.M.R. Peres, F. Guinea, Phys. Rev. B 76 (2007) 205423.
[56] S. Ahmed, M.G. Rasul, R. Brown, et al., J. Environ. Manage. 92 (2011) 311–330.
[57] S.J. Jiao, S.R. Zheng, D.Q. Yin, et al., Chemosphere 73 (2008) 377–382.
[58] F. Saadati, N. Keramati, M.M. Ghazi, Crit. Rev. Env. Sci. Tec. 46 (2016) 757–782.
[59] R.F. Yuan, Y.D. Zhu, B.H. Zhou, et al., Chem. Eng. J. 359 (2019) 1527–1536.
[60] L.Y. Wu, Z.Q. Sun, Y.F. Zhen, et al., Environ. Sci. Technol. 55 (2021) 15400–15411.
[61] S.S. Zhu, X.J. Li, J. Kang, et al., Environ. Sci. Technol. 53 (2018) 307–315.